



HAL
open science

SOHO SWAN Ly α Models Supporting LRO LAMP: 2008–2023

Wayne R Pryor, W Kent Tobiska, Kurt D Retherford, Cesare Grava, Anthony Egan, Thomas K Greathouse, G Randall Gladstone, Eric Quémerais

► **To cite this version:**

Wayne R Pryor, W Kent Tobiska, Kurt D Retherford, Cesare Grava, Anthony Egan, et al.. SOHO SWAN Ly α Models Supporting LRO LAMP: 2008–2023. *The Planetary Science Journal*, 2024, 5 (9), pp.210. 10.3847/psj/ad7502 . insu-04716689

HAL Id: insu-04716689

<https://insu.hal.science/insu-04716689v1>

Submitted on 1 Oct 2024

HAL is a multi-disciplinary open access archive for the deposit and dissemination of scientific research documents, whether they are published or not. The documents may come from teaching and research institutions in France or abroad, or from public or private research centers.






L'archive ouverte pluridisciplinaire **HAL**, est destinée au dépôt et à la diffusion de documents scientifiques de niveau recherche, publiés ou non, émanant des établissements d'enseignement et de recherche français ou étrangers, des laboratoires publics ou privés.



Distributed under a Creative Commons Attribution 4.0 International License



SOHO SWAN Ly α Models Supporting LRO LAMP: 2008–2023

Wayne R. Pryor^{1,2} , W. Kent Tobiska¹, Kurt D. Retherford^{3,4} , Cesare Grava³ , Anthony Egan⁵, Thomas K. Greathouse³ ,
G. Randall Gladstone^{3,4} , and Eric Quémerais⁶

¹ Space Environment Technologies, LLC, 528 Palisades Drive, Ste 164, Pacific Palisades, CA 90272-2844, USA

² Science and Engineering Division, Central Arizona College, 8470 N. Overfield Road, Coolidge, AZ 85128, USA

³ Southwest Research Institute, 6220 Culebra Road, San Antonio, TX 78238, USA

⁴ University of Texas at San Antonio, One UTSA Circle, San Antonio, TX 78849, USA

⁵ Southwest Research Institute, 1050 Walnut Street #300, Boulder, CO 80302, USA

⁶ LATMOS-OVSQ, Université Versailles Saint-Quentin, Guyancourt, France

Received 2024 April 19; revised 2024 August 22; accepted 2024 August 27; published 2024 September 30

Abstract

The Lunar Reconnaissance Orbiter Lyman-Alpha Mapping Project (LAMP) has been mapping the Moon since its launch in 2009. Faint ultraviolet illumination of the lunar dark side includes light from stars and from hydrogen Ly α emissions, mostly attributed to sunlight scattered by hydrogen atoms near the Sun with a smaller contribution from the whole Galaxy. Models of the lunar illumination by time-dependent Ly α photons have allowed the LAMP team to map polar shadowed craters suspected of harboring water ice and other volatiles. This paper describes the model that provides daily all-sky Ly α maps tuned by comparisons with all-sky Ly α maps from the Solar and Heliospheric Observatory Solar Wind ANisotropy Experiment stationed at the Sun–Earth L1 point.

Unified Astronomy Thesaurus concepts: [Heliosphere \(711\)](#)

1. Introduction

The Lunar Reconnaissance Orbiter (LRO; G. Chin et al. 2007; R. Vondrak et al. 2010; J. W. Keller et al. 2016) has been mapping the lunar surface from low polar orbit since orbit insertion on 2009 June 23. The usually nadir-viewing Lyman-Alpha Mapping Project (LAMP; G. R. Gladstone et al. 2010) instrument contains an ultraviolet spectrograph (57–196 nm wavelength) collecting time-tagged photons coming from the lunar surface. The LAMP team is studying permanently shadowed regions (PSRs), polar craters that stay in darkness and may contain water ice and other lunar volatiles. Lunar nightside illumination is modeled as a combination of starlight and time-dependent heliospheric Ly α produced by sunlight scattering from interstellar wind hydrogen atoms passing through the solar system. LAMP mapping found that PSR regions are darker at all far-ultraviolet (FUV) wavelengths than non-PSR regions, and this phenomenon is attributed to higher soil porosity (G. R. Gladstone et al. 2012; B. Byron et al. 2019). Spectral studies of the PSRs from LAMP have found that they are redder than non-PSR regions, indicating absorption features from water ice and other volatiles (G. R. Gladstone et al. 2012; P. O. Hayne et al. 2015; L. O. Magaña et al. 2022, 2023).

This paper discusses the time-dependent Ly α illumination model used by the LAMP team. An earlier report (W. R. Pryor et al. 2013) detailed this model that provides daily all-sky Ly α maps appropriate for the vicinity of the Moon that have been tuned to fit Solar Heliospheric Observatory (SOHO) Solar Wind Anisotropy Experiment (SWAN; J. L. Bertaux et al. 1995) maps obtained from the Sun–Earth L1 point. Those all-sky Ly α maps are then used to estimate the illumination for each point on the Moon as part of the LAMP lunar mapping pipeline.

Here we describe updated models to use in future lunar maps, based on several developments. First, roughly one solar cycle has passed, allowing us to look for issues in the time-dependent model and/or degradation of the SWAN detector. Second, nine different models were computed for each day of the mission, to select the best-fitting solar wind latitudinal profile and improve the illumination estimates. Third, recent studies of Ly α data from the Voyager, New Horizons, Pioneer, and Cassini spacecraft (O. A. Katushkina et al. 2017; G. R. Gladstone et al. 2018, 2021; W. R. Pryor et al. 2022, 2024) suggest that the heliospheric Ly α models should include a substantial Galactic contribution, that we treat as a constant, isotropic background of 43 *Rayleigh* (*R*). Finally, E. Quémerais (2024, private communication) has recently provided a revised SWAN absolute calibration based on a cross-calibration with the “Probing of the Hermean Exosphere by Ultraviolet Spectroscopy” (PHEBUS) instrument on the Bepi-Colombo Mercury Planetary Orbiter (E. Chassefière et al. 2010; E. Quémerais et al. 2020) and a SWAN degradation curve based on stellar observations.

2. Data Sets

The SOHO SWAN (J. L. Bertaux et al. 1995; E. Quémerais & J.-L. Bertaux 2002) instrument uses a dual periscope mechanism to obtain regular all-sky Ly α maps with FUV 5 × 5 array detectors with 1° × 1° field-of-view pixels sensitive to light from 115 to 180 nm wavelength. The detectors also record light from many stars, concentrated near the Galactic plane. Small regions near the Sun and around the spacecraft are excluded from the all-sky maps. Initial SWAN results were presented in J. L. Bertaux et al. (1997), emphasizing the enhanced solar wind charge exchange removing slow interstellar hydrogen atoms near the ecliptic plane, leading to a dark “groove” at solar minimum conditions. SWAN data has enabled detailed determination of the solar wind mass flux latitudinal asymmetries and their



Original content from this work may be used under the terms of the [Creative Commons Attribution 4.0 licence](#). Any further distribution of this work must maintain attribution to the author(s) and the title of the work, journal citation and DOI.

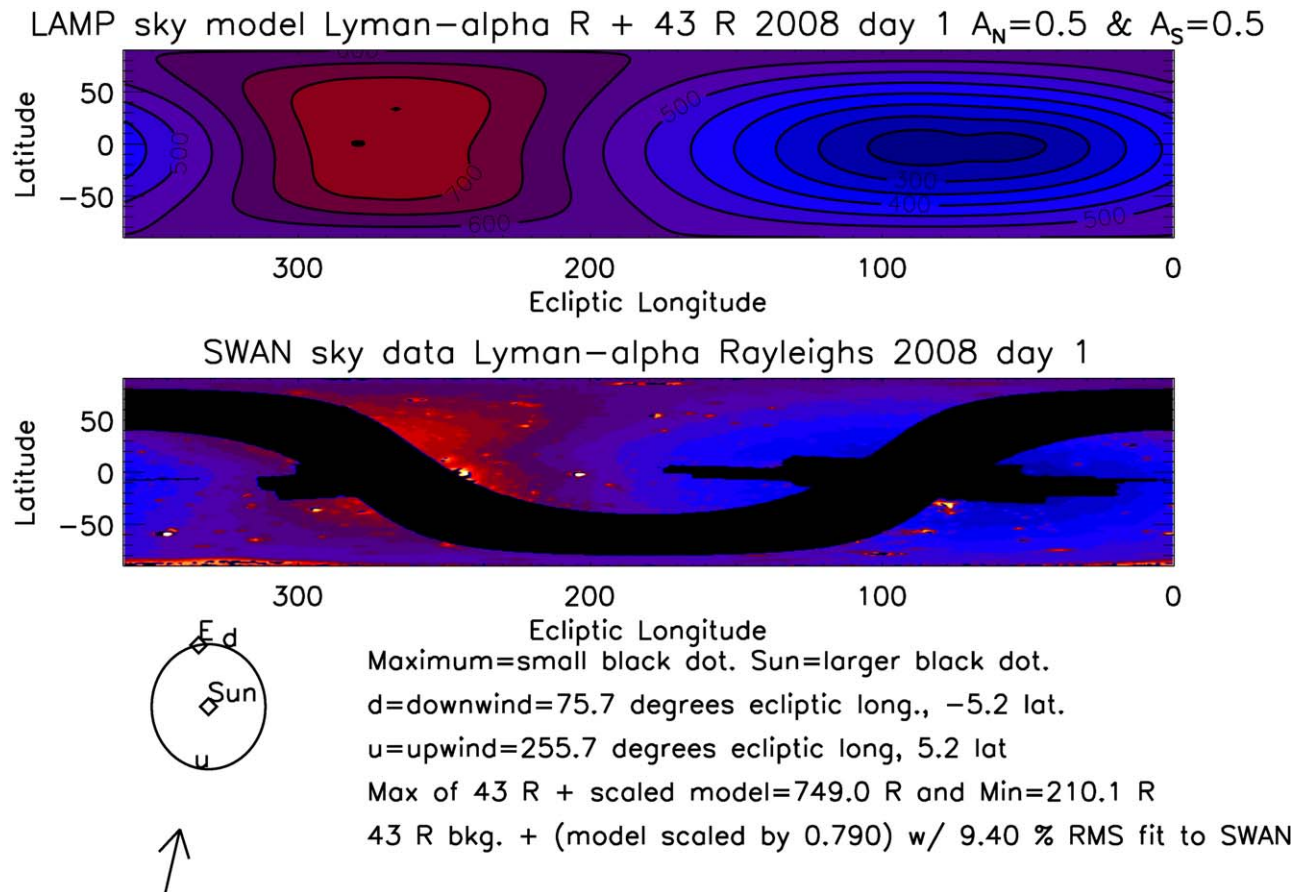


Figure 1. Sample SWAN all-sky Ly α map for 2008 January 1 (bottom) and a corresponding scaled heliospheric model, with an added 43 R of isotropic Galactic background with charge-exchange lifetime asymmetry parameter $A = 0.5$ in both N and S hemispheres, indicated as $A_N = 0.5$ and $A_S = 0.5$ (top). Contour lines are 50 R apart. The small figure at the lower left illustrates the position of the Earth (E) in its orbit around the Sun with respect to the interstellar wind flow, indicated by an arrow, and upwind (u) and downwind (d) indicators.

variations (E. Quémerais et al. 2008; O. A. Katushkina et al. 2013; D. Koutroumpa et al. 2019).

The SWAN instrument continues to regularly obtain these Ly α maps, which have been provided to us by the SWAN team for the purpose of checking our daily lunar illumination models used for LRO LAMP lunar mapping. The SWAN maps for 2008–2023 were provided in *Rayleighs* (R) by the SWAN team and assumed a constant instrument sensitivity of 4.1 R per (count per second). A cross-calibration of PHEBUS with SWAN in 2020 finds that instead of the SWAN sensitivity of 4.1 R per (count per second) used in the existing data files from 2001 to 2023, SWAN in 2020 had a sensitivity of 3.8 R per (count per second). Including the effects of the new stellar degradation curve (to be shown in Figure 3), this suggests an initial SWAN sensitivity of 3.2 R per (count per second). That is, after correcting for the degradation, and using this cross-calibration with PHEBUS, in future work SWAN intensities should be divided by a factor of 1.28. We will use this revised initial calibration in this paper. The modeling section will examine the model fits both with and without the new SWAN stellar degradation curve. Figure 1 is a sample SWAN map as provided by the SWAN team, then scaled down in intensity by 1.28 and corrected for degradation, along with the corresponding best-fitting model. Points near the Galactic plane and obvious UV-bright O and B stars have been filtered from the data before comparison with models. Thirteen days of SWAN data were excluded from the results shown here due to obvious

issues in the collected data sets and/or corresponding geometry, perhaps due to telemetry problems.

3. Model

We used a standard heliospheric hot model (G. E. Thomas 1978; J. M. Ajello et al. 1987, 1994; W. R. Pryor et al. 1992, 1998, 2013, 2020, 2022, 2024) to describe the interstellar wind hydrogen passing through the solar system and illuminated by sunlight. The models assumed an inflow of interstellar wind neutral hydrogen from the upwind direction 254°7 ecliptic longitude and 5°2 ecliptic latitude based on measurements of the well-defined helium focusing cone by the Ulysses GAS instrument (M. Witte 2004). Note that Witte used B1950 coordinates, while in J2000 coordinates the corresponding ecliptic longitude is 255°7 (E. Möbius et al. 2012), used in this paper. We have neglected the slight offset in the hydrogen flow direction from the helium flow direction found in SOHO SWAN data (R. Lallement et al. 2005). Hydrogen thermodynamic parameters used in the hot model just inside the termination shock included a density $n = 0.12 \text{ cm}^{-3}$, velocity $v = 20 \text{ km s}^{-1}$, and temperature $T = 12,000 \text{ K}$ (for discussions of v and T see, e.g., J. T. Clarke et al. 1998 and J. Costa et al. 1999).

The time-dependent Ly α line-integrated flux is taken from the Laboratory for Atmospheric and Space Physics (LASP) solar database (T. N. Woods et al. 2000), with a correction to the estimated line-center flux (C. Emerich et al. 2005;

Table 1
Mean A -value of the Best-fitting Model by Year

Year:	2008	2009	2010	2011	2012	2013	2014	2015	2016	2017	2018	2019	2020	2021	2022	2023
A -value:	0.48	0.55	0.54	0.49	0.32	0.20	0.23	0.40	0.40	0.45	0.44	0.39	0.46	0.63	0.66	0.48

P. Lemaire et al. 2015; M. Kretschmar et al. 2018). The major loss process for slow hydrogen near the Sun is charge exchange with solar wind protons. Solar wind proton density and velocity data is taken from the National Space Science Data Center database (J. H. King & N. E. Papitashvili 2005). The solar-wind charge-exchange lifetime t has a variation in heliographic latitude that is estimated using a solar wind asymmetry parameter A , with the A parameter defined by the expression

$$t(\text{latitude}) = t(\text{latitude} = 0)/(1 - A\sin^2(\text{latitude})),$$

which leads to a larger lifetime away from the ecliptic plane for positive values of A (e.g., N. Witt et al. 1979). For the case $A = 0.0$, the hydrogen lifetime against charge exchange t is isotropic, while for $A = 0.5$ the hydrogen atom lifetime is twice as long at the pole as at the equator. A secondary loss process for hydrogen atoms is time-dependent EUV photoionization, which is estimated using the Space Environment Technologies Solar Irradiance Program (W. K. Tobiska et al. 2000; W. K. Tobiska & S. D. Bouwer 2006).

The radiative transfer model used is fundamentally a single scattering model. However, a correction is made for multiple scattering enhancement of signal in the downwind direction based on the angle formed between a ray from the Sun to upwind and a ray from the Sun to the scattering point, as discussed in E. Quémerais & J.-L. Bertaux (1993), J. M. Ajello et al. (1994), and W. R. Pryor et al. (1998) and calculated using multiple scattering codes (D. T. Hall 1992; D. T. Hall et al. 1993).

This paper fits the SWAN Ly α data from each map with a representation of the form:

$$\text{Data} = \text{galactic Ly}\alpha \text{ background} \\ + \text{scale factor} \times (\text{heliospheric Ly}\alpha \text{ model}).$$

In this paper, we use a constant Galactic background of 43 R found from New Horizons outer heliospheric Ly α data by G. R. Gladstone et al. (2021). The scale factor for a particular data set is found from the expression:

$$\text{Scale factor} \\ = \sum(\text{Data-galactic Ly}\alpha \text{ background})/\sum \text{heliospheric model},$$

where the \sum represents a sum over the filtered data points being studied. Also important is the rms fit between the filtered data and the model, defined in W. R. Pryor et al. (2022). We choose among various possible models by minimizing the rms fit.

In W. R. Pryor et al. (2013) we produced Ly α models for 2008–2011 using $A_N = 0.8$ and $A_S = 0.5$ based on a single two-parameter fit to a MESSENGER Mercury Atmospheric and Surface Composition Spectrometer (MASCS) Ly α map obtained from 2009 to 2011, with A_N and A_S representing the northern and southern solar hemispheres, and compared the models to all-sky heliospheric Ly α maps produced by the SOHO SWAN experiment. In the early years of the LRO mission, the data/model ratio was declining in time, consistent with SWAN instrumental degradation with time. Therefore, we used the model

directly in the lunar illumination pipeline, without scaling the model to the SWAN data. However, in recent years, the data/model ratio using fixed values of A has recovered to nearly its initial value, suggesting a possible solar cycle variation issue in the model in addition to any SWAN degradation after 2008. To explore a possible time dependence in the solar wind asymmetry, we ran a set of nine models of the SWAN data for each day from 2008 to 2023 with solar wind asymmetry parameter values of $A = 0.0, 0.1, 0.2, \dots, 0.8$. For each year, we found the best-fitting model of the degradation-corrected SWAN data from this set (Table 1), using the two expressions given above. Note that we have assumed the same asymmetry parameter in each solar hemisphere to minimize the computational requirements. Running the nine models described with the same asymmetry parameter in each hemisphere ($A = 0.0, 0.1, \dots, 0.8$) on the large set of SWAN data from 2008 to 2023 takes several months on our current computers. The 81 models of a better two-parameter version ($A_N = 0, A_S = 0; A_N = 0, A_S = 0.1; \dots$) would take an excessive length of time.

For most years the best-fitting model found was for $A = 0.4$ or $A = 0.5$, appropriate for solar minimum conditions with enhanced solar wind mass flux near the ecliptic plane. For the 2008 solar minimum case shown in Figure 1, the $A = 0.5$ model provided the best fit to the data. However, for the three years 2012, 2013, and 2014, near solar maximum, the three corresponding best-fitting models were $A = 0.3, 0.2,$ and 0.2 , respectively, consistent with more isotropic solar wind at solar maximum. This expected behavior, however, did not persist into the current ongoing solar maximum, with the best-fitting models in 2022 and 2023 having $A = 0.7$ and 0.5 , respectively. Table 1 shows the mean A value found for each year of data, while Figure 2 is a plot of the best-fitting A value for each map, showing the significant scatter within a year, along with a plot of the mean A value for each year.

To assess the relative A values in the north and south, Figure 2 also contains the mean A value for each year for SWAN data points looking north of the ecliptic plane (triangles), and the mean A value for SWAN data points looking south of the ecliptic plane (X symbols). The most obvious feature in the north–south behavior is more solar wind mass flux isotropy (lower A values) in the north than in the south in the previous solar maximum, especially near 2013. This north–south behavior can also be seen in the retrievals of Figure 2 of O. Katushkina et al. (2019). A second check on the north versus south results is to look at the period from 2008 to 2011 when MESSENGER MASCS cruise observations modeled by a two-parameter fit found $A_N = 0.8, A_S = 0.5$ (W. R. Pryor et al. 2013). Figure 2 of this paper does show the currently derived A value in that period is slightly higher in the north compared to the south in the SWAN modeling but with a smaller difference than in the 2013 paper.

Next, we examined the time dependence of the rms fits to the adjusted SWAN data along with two kinds of scale factors in the second, third, and fifth panels of Figure 3. The first scale factor shown in the third panel is for the case where the relative

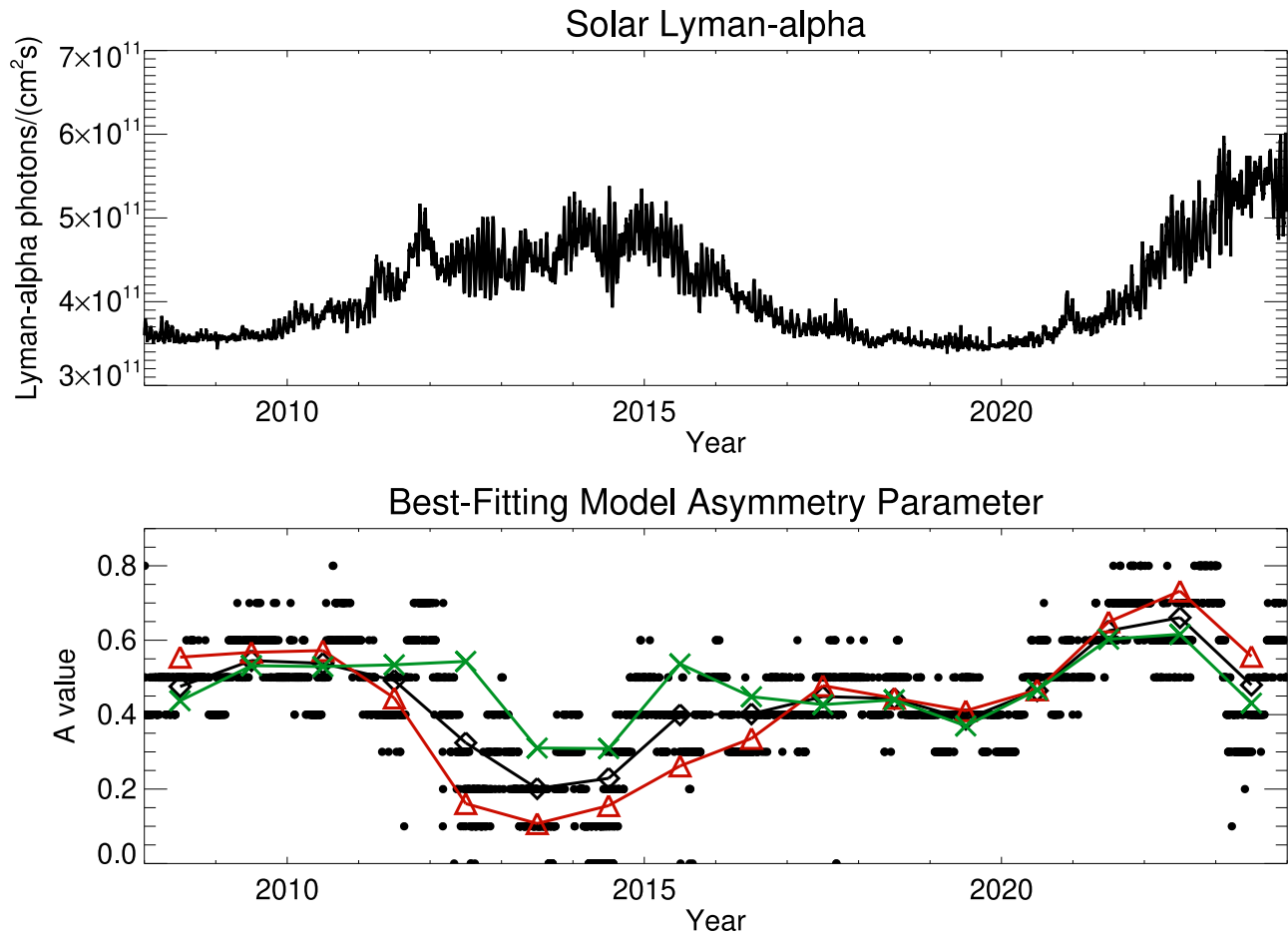


Figure 2. Top: solar Ly α line-integrated flux used as a model input at 1 au from the Sun for 2008–2023. Bottom: the value of the asymmetry parameter A of the best-fitting model for the SWAN data is shown as a function of time. Each dot is the daily best-fitting model; each diamond is the annually averaged best-fitting model. The annually averaged best-fitting models for points in the northern and in the southern hemispheres are shown with red triangles and green X symbols, respectively. A $43 R$ constant Galactic background was added to the scaled heliospheric model before fitting.

degradation from the star data is not included in the data, but the SWAN data files have been divided by a factor of 1.28. The fourth panel shows the relative response of SWAN found in stellar calibrations. The revised scale factors shown in the fifth panel include both the 1.28 factor and the relative degradation indicated by the stellar calibrations. The rms fits and both kinds of scale factors are shown for a case with a constant asymmetry factor of $A = 0.5$ for all years. Also shown is a case where the model with the best-fitting asymmetry factor is used for each year. For example, $A = 0.5$ was used in 2009 and 2010, $A = 0.4$ in 2011, etc., based on the results in Table 1. In this case, the scale factor is slightly more constant and the rms fits are slightly lower, indicating that this is a better way to capture the solar-cycle variations in lunar illumination that can then be used in the LAMP lunar mapping pipeline. The largest improvement is seen near the solar maximum of 2013–2015 where the rms fit is reduced from about 10% to 9% when the derived asymmetry parameter was significantly lower.

From looking at the overall trend of the scale factors found in the third panel we see a decline in the scale factors, from initial values near 0.8 to values near 0.4 at the end of the observations, suggesting declining SWAN sensitivity. The fourth panel, showing the relative response of SWAN to starlight, also indicates declining SWAN sensitivity with time, in this case by about 20%. The final panel, where the SWAN data have been corrected for the declining sensitivity shown in

the fourth panel, removes the overall degradation trend. The revised scale factors in the final panel span a smaller range of values (about 0.8–0.6) than those in the third panel, indicating that the correction for degradation is working and the revised scale factors should be used in future lunar maps. If the hot model were perfectly accurate, and the SWAN data were now perfectly calibrated, the revised scaling factor would be constant throughout the solar cycle. The linear fit to the scale factors of the best-fitting model in the third panel starts at 0.699 in 2008 and has a downward slope of -0.0085 yr^{-1} . Including the stellar degradation curve, the linear fit to the revised scale factors starts at 0.745 in 2008 with a greatly reduced slope of -0.0017 yr^{-1} , providing an almost flat dashed line in the fifth panel, and is much closer to the ideal constant value.

Examination of the residual variations in the revised scale factor plot in the fifth panel indicates an anticorrelation with the line-integrated solar Ly α flux shown in the top panel, which we interpret as issues in the modeling of related quantities such as the assumed line-center flux illuminating the hydrogen atoms and the associated radiation pressure pushing the hydrogen atoms.

4. Discussion

Our future LAMP lunar mapping activities will use the best-fitting heliospheric Ly α model found for each year. The

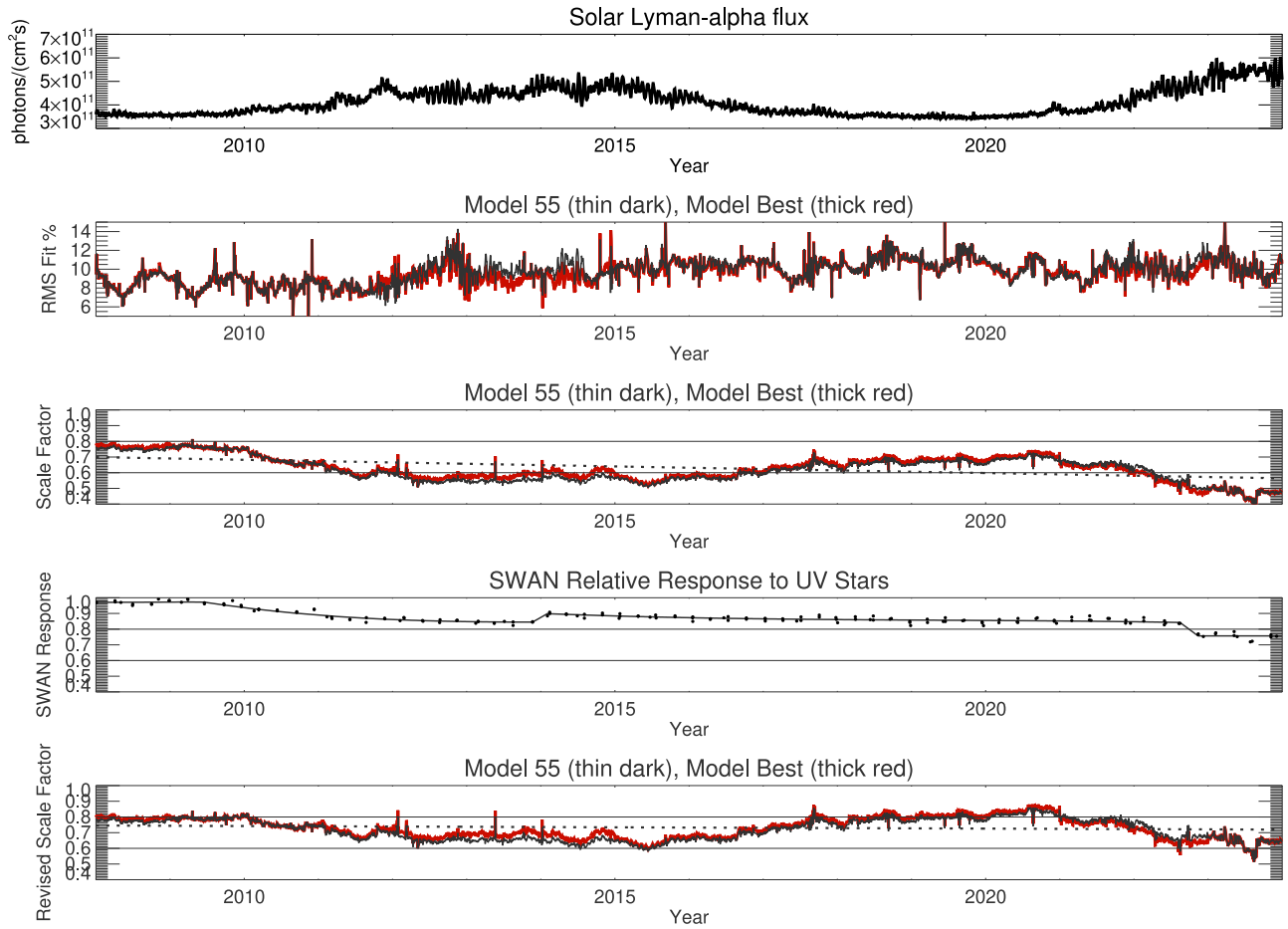


Figure 3. Top panel: solar Ly α line-integrated flux used as a model input at 1 au from the Sun for 2008–2023. Second panel: rms % fit (middle) to the adjusted SWAN data for the $A = 0.5$ model (model 55, thin dark line) and for the model formed from using the best-fitting model for each year (thick red line). Third panel: scale factors derived for the SWAN data files (divided by 1.28) to multiply by the heliospheric model before adding a $43 R$ galactic background to estimate the illumination of the lunar dark side. Thin horizontal lines have been added at 0.6 and 0.8 to guide the eye. The dashed line is a linear fit to the scale factors for the best-fitting model. Fourth panel: the relative response of the SWAN detector to UV stars over the mission. Individual measurements are shown as round dots, along with a piece-by-piece fit to those measurements, preserving two apparent steps in that data. Fifth panel: revised scale factors derived for the fully degradation-adjusted SWAN data values to multiply by the heliospheric model before adding a $43 R$ galactic background to better estimate the illumination of the lunar dark side. The dashed line is a linear fit to the revised scale factors for the best-fitting model.

derived revised scale factors (stored in a separate IDLsave file) will be multiplied by the calculated model values before adding a Galactic background of $43 R$ to these values to obtain the Ly α sky brightness values used to estimate the lunar dark side Ly α illumination.

Knowing the correct heliospheric hydrogen density value is important for at least two reasons. First, running standard Ly α models with that density permits intercalibration of UV instruments at a variety of locations and look directions in the solar system. Second, charge exchange between interstellar neutral hydrogen and solar wind protons slows the solar wind flow, and that, in turn, affects the size of the heliosphere. The density value of $n = 0.12 \text{ cm}^{-3}$ “at infinity” used in the hydrogen hot model runs described here is not particularly well constrained. W. R. Pryor et al. (2024) found a hydrogen density of $n = 0.14 \pm 0.03 \text{ cm}^{-3}$ based on the Cassini UVIS laboratory calibration (L. W. Esposito et al. 2004). This density value should be understood as the upwind hydrogen density just inside of the solar wind termination shock. P. Swaczyna et al. (2020) found a similar neutral hydrogen density at the termination shock $n_{\text{H,TS}} = 0.127 \pm 0.015 \text{ cm}^{-3}$ from their models of New Horizons Solar Wind Around Pluto data. Errors in laboratory calibration, instrument changes, and

modeling errors are all part of the significant uncertainty in the derived densities for various spacecraft.

The two kinds of scaling factors shown in Figure 3 can be considered as adjustment factors on the hot model hydrogen density, taken to be 0.12 cm^{-3} in the model runs presented here, since the model brightnesses change roughly linearly with changes in hydrogen density. The scaling factors for the best-fitting model in the third panel of Figure 3 have an average scale factor of 0.610 ± 0.077 . This would correspond to a hydrogen density in the hot model of about $0.12 \times 0.61 = 0.073 \text{ cm}^{-3}$. The revised scaling factors for the best-fitting model in the fifth panel of Figure 3 for the data including the stellar degradation correction have a larger average revised scale factor of 0.709 ± 0.072 . This would correspond to a hydrogen density in the hot model of about $0.12 \times 0.709 = 0.085 \text{ cm}^{-3}$.

Next, we describe the SWAN team’s current understanding of the heliospheric hydrogen density based on their modeling of PHEBUS data (E. Quémerais 2023, private communication). As described earlier, PHEBUS data was used to provide the SWAN calibration used in this paper. V. V. Izmodenov et al. (2013) and V. V. Izmodenov & D. B. Alexashov (2015) presented a heliospheric hydrogen model including outer

heliospheric effects such as filtration not included in the hot models described in this paper. Applying that model to 2020 March observations from the more recently calibrated PHEBUS instrument on the Bepi-Colombo Mercury Planetary Orbiter (E. Chassefière et al. 2010; E. Quémerais et al. 2020) leads to a new estimate of the interplanetary hydrogen inside the termination shock of $n_H = 0.09 \text{ cm}^{-3}$. (According to the Izmodenov model, this corresponds to an unfiltered interstellar value of $n_H = 0.12 \text{ cm}^{-3}$ in the undisturbed interstellar medium well upstream of the heliopause, heliosheath, and termination shock.) The PHEBUS-based density value inside the termination shock of $n_H = 0.09 \text{ cm}^{-3}$ is quite close to the revised scaled density of about 0.085 cm^{-3} found using the hot model to examine SWAN data in this study.

The interplanetary hydrogen densities near 0.09 cm^{-3} favored by the SWAN team in the previous paragraph and found in our work here with the new SWAN calibration are significantly lower than the hydrogen density value of $n_H = 0.14 \pm 0.03 \text{ cm}^{-3}$ found based on the Cassini UVIS lab calibration in W. R. Pryor et al. (2022), with the density differences ultimately traceable to differences in absolute laboratory calibrations. Finally, we note that Cassini UVIS and MESSENGER MASCs were both calibrated at the University of Colorado LASP, but applying our hot model with a hydrogen density of 0.12 cm^{-3} to MASCs interplanetary Ly α data required a scale factor of 0.62 (W. R. Pryor et al. 2013), suggesting the MASCs calibration is consistent with a hydrogen density of $0.12 \times 0.62 = 0.074 \text{ cm}^{-3}$, more in line with the SWAN and PHEBUS hydrogen density determinations near 0.09 cm^{-3} discussed above. The large difference in the measured brightnesses from the two LASP-calibrated instruments, MESSENGER MASCs and the Cassini UVIS, may be a result of larger-than-expected calibration systematic errors. Alternatively, the instrument calibrations may have drifted after laboratory calibration during storage, ground transportation, launch into space, and exposure to the changing conditions of the space environment near a new operating spacecraft.

5. Conclusions

This paper documents the heliospheric Ly α modeling to be used in future LRO LAMP lunar mapping, including more than one solar cycle of daily modeling. Estimates of the solar cycle dependence of the solar-wind asymmetry parameter were provided in Table 1 and Figure 2. The use of the average asymmetry parameter for each year has improved the lunar illumination model over a model with a constant asymmetry parameter. A Galactic background is now included in the modeling based on the work of G. R. Gladstone et al. (2021). Finally, incorporating a cross-calibration with PHEBUS and stellar measurements of the time-dependent SWAN calibration will improve future LAMP lunar Ly α maps. LRO and the LAMP instrument continue to operate and obtain lunar maps that will prove useful for future exploration of the lunar polar regions.

Acknowledgments

Eric Quémerais and Stéphane Ferron provided the set of calibrated SOHO SWAN maps and the most recent calibration adjustments. W.P. and K.T. acknowledge ongoing support for hydrogen Ly α modeling studies from the NASA LRO Lyman-

Alpha Mapping Project (LAMP) team at Southwest Research Institute (SwRI) through a subcontract to Space Environment Technologies (SET). W.P. also acknowledges ongoing support from Central Arizona College.

ORCID iDs

Wayne R. Pryor  <https://orcid.org/0000-0001-8112-8783>
 Kurt D. Retherford  <https://orcid.org/0000-0001-9470-150X>
 Cesare Grava  <https://orcid.org/0000-0003-2886-6159>
 Thomas K. Greathouse  <https://orcid.org/0000-0001-6613-5731>
 G. Randall Gladstone  <https://orcid.org/0000-0003-0060-072X>

References

- Ajello, J. M., Pryor, W. R., Barth, C. A., et al. 1994, Observations of Interplanetary Lyman- α with the Galileo Ultraviolet Spectrometer: Multiple Scattering Effects at Solar Maximum, *A&A*, **289**, 283
- Ajello, J. M., Stewart, A. I., Thomas, G. E., & Graps, A. 1987, Solar Cycle Study of Interplanetary Lyman- α Variations: Pioneer Venus Orbiter Sky Background Results, *ApJ*, **317**, 964
- Bertaux, J. L., Kyrölä, E., Quémerais, E., et al. 1995, SWAN: A Study of Solar Wind Anisotropies on SOHO with Lyman Alpha Sky Mapping, *SoPh*, **162**, 403
- Bertaux, J. L., Quémerais, E., Lallement, R., et al. 1997, First Results from SWAN Lyman α Solar Wind Mapper on SOHO, *SoPh*, **175**, 737
- Byron, B. D., Retherford, K. D., Mandt, K. E., et al. 2019, Porosity Maps of the Lunar Surface Derived from LRO-LAMP Albedo Data, *LPS*, **50**, 3115
- Chassefière, E., Maria, J.-L., Goutail, J.-P., et al. 2010, PHEBUS: A Double Ultraviolet Spectrometer to Observe Mercury's Exosphere, *P&SS*, **58**, 201
- Chin, G., Brylow, S., Foote, M., et al. 2007, Lunar Reconnaissance Orbiter Overview: The Instrument Suite and Mission, *SSRv*, **129**, 391
- Clarke, J. T., Lallement, R., Bertaux, J.-L., et al. 1998, HST/GHRS Observations of the Velocity Structure of Interplanetary Hydrogen, *ApJ*, **499**, 482
- Costa, J., Lallement, R., Quémerais, E., et al. 1999, Heliospheric Interstellar H Temperature from SOHO/SWAN H Cell Data, *A&A*, **349**, 660
- Emerich, C., Lemaire, P., Vial, J.-C., et al. 2005, A New Relation between the Central Spectral Solar H I Lyman α Irradiance and the Line Irradiance Measured by SUMER/SOHO During the Cycle 23, *Icar*, **178**, 429
- Esposito, L. W., Barth, C. A., Colwell, J. E., et al. 2004, The Cassini Ultraviolet Imaging Spectrograph Investigation, *SSRv*, **115**, 299
- Gladstone, G. R., Pryor, W. R., Hall, D. T., et al. 2021, New Horizons Detection of the Local Galactic Lyman- α Background, *AJ*, **162**, 241
- Gladstone, G. R., Pryor, W. R., Stern, S. A., et al. 2018, The Lyman- α Sky Background as Observed by New Horizons, *GeoRL*, **45**, 8022
- Gladstone, G. R., Retherford, K. D., Egan, A. F., et al. 2012, Far-ultraviolet Reflectance Properties of the Moon's Permanently Shadowed Regions, *JGRE*, **117**, E00H04
- Gladstone, G. R., Stern, S. A., Retherford, K. D., et al. 2010, LAMP: The Lyman Alpha Mapping Project on NASA's Lunar Reconnaissance Orbiter Mission, *SSRv*, **150**, 161
- Hall, D. T. 1992, Ultraviolet Resonance Line Radiation and the Structure of the Heliosphere, PhD thesis, Univ. Arizona
- Hall, D. T., Shemansky, D. E., Judge, D. L., Gangopadhyay, P., & Gruntman, M. A. 1993, Heliospheric Hydrogen Beyond 15 AU: Evidence for a Termination Shock, *JGR*, **98**, 15185
- Hayne, P. O., Hendrix, A., Sefton-Nash, E., et al. 2015, Evidence for Exposed Water Ice in the Moon's South Polar Regions from Lunar Reconnaissance Orbiter Ultraviolet Albedo and Temperature Measurements, *Icar*, **255**, 58
- Izmodenov, V. V., & Alexashov, D. B. 2015, Three-Dimensional Kinetic-MHD Model of the Global Heliosphere with the Heliopause-Surface Fitting, *ApJS*, **220**, 32
- Izmodenov, V. V., Katushkina, O. A., Quémerais, E., & Bzowski, M. 2013, Distribution of Interstellar Hydrogen Atoms in the Heliosphere and Backscattered Solar Lyman- α , in Cross-calibration of Far-UV Spectra of Solar System Objects and the Heliosphere, ed. E. Quémérais, M. Snow, & R. M. Bonnet (New York: Springer), 7
- Katushkina, O., Izmodenov, V., Koutroumpa, D., Quémérais, E., & Jian, L. K. 2019, Unexpected Behavior of the Solar Wind Mass Flux During Solar Maxima: Two peaks at Middle Heliolatitudes, *SoPh*, **294**, 17

- Katashkina, O. A., Izmodenov, V. V., Quémerais, E., & Sokól, J. M. 2013, Heliolatitude and Time Variations of the Solar Wind Mass Flux: Inferences from the Backscattered Solar Lyman- α Intensity Maps, *JGRA*, **118**, 2800
- Katashkina, O. A., Quémerais, E., Izmodenov, V. V., Lallement, R., & Sandel, B. R. 2017, Voyager 1/UVS Lyman α Measurements at the Distant Heliosphere (90-130 AU): Unknown Source of Additional Emission, *JGRA*, **122**, 10921
- Keller, J. W., Petro, N. E., & Vondrak, R. R. 2016, The Lunar Reconnaissance Orbiter Mission- Six years of Science and Exploration at the Moon, *Icar*, **273**, 2
- King, J. H., & Papitashvili, N. E. 2005, Solar Wind Spatial Scales in and Comparisons of Hourly Wind and ACE Plasma and Magnetic Field Data, *JGRA*, **110**, A02104
- Koutroumpa, D., Quemerai, E., Ferron, S., & Schmidt, W. 2019, Global Distribution of the Solar Wind Flux and Velocity From SOHO/SWAN During SC-23 and SC-24, *GeoRL*, **46**, 4114
- Kretschmar, M., Snow, M., & Curdt, W. 2018, An Empirical Model of the Variation of the Solar Lyman- α Spectral Irradiance, *GeoRL*, **45**, 2138
- Lallement, R., Quemerai, E., Bertaux, J. L., et al. 2005, Deflection of the Interstellar Neutral Hydrogen Flow Across the Heliospheric Interface, *Sci*, **307**, 1447
- Lemaire, P., Vial, J.-C., Curdt, W., Schühle, U., & Wilhelm, K. 2015, Hydrogen Ly- α and Ly- β Full Sun Line Profiles Observed with SUMER/SOHO (1996-2009), *A&A*, **581**, A26
- Magaña, L. O., Retherford, K. D., Byron, B. D., et al. 2022, LRO-LAMP Survey of Lunar South Pole Cold Traps: Implication for the Presence of Condensed H₂O, *JGRE*, **127**, e2022JE007301
- Magaña, L. O., Retherford, K. D., Byron, B. D., et al. 2023, LRO-LAMP Lunar South Pole Cold Traps: Assessment of H₂O and Potential CO₂ and NH₃ Reserves, *JGRE*, **128**, e2023JE007863
- Möbius, E., Bochsler, P., Bzowski, M., et al. 2012, Interstellar Gas Flow Parameters Derived from Interstellar Boundary Explorer-Lo Observations in 2009 and 2010: Analytical Analysis, *ApJS*, **198**, 11
- Pryor, W. R., Ajello, J. M., Barth, C. A., et al. 1992, The Galileo and Pioneer Venus Ultraviolet Spectrometer Experiments: Solar Lyman- α Latitude Variation at Solar Maximum from Interplanetary Lyman- α Observations, *ApJ*, **394**, 363
- Pryor, W. R., Lasica, S. J., Stewart, A. I. F., et al. 1998, Interplanetary Lyman α Observations from Pioneer Venus over a Solar Cycle from 1978 to 1992, *JGR*, **103**, 26833
- Pryor, W. R., Holsclaw, G. M., McClintock, W. E., et al. 2013, Lyman- α Models for LRO LAMP from MESSENGER MASCS and SOHO SWAN data, in Cross-calibration of Far-UV Spectra of Solar System Objects and the Heliosphere, ed. E. Quémerais, M. Snow, & R. M. Bonnet (New York: Springer), 163
- Pryor, W. R., Tobiska, W. K., Retherford, K. D., et al. 2020, Models of Heliospheric Lyman-Alpha in Support of LRO LAMP, LPSC, **51**, 1665
- Pryor, W. R., Gladstone, G. R., Retherford, K. D., & Tobiska, W. K. 2022, Supporting Evidence for a Galactic Ly α Background from Cassini UVIS Data, *AJ*, **164**, 46
- Pryor, W. R., Gladstone, G. R., Retherford, K. D., et al. 2024, Modeling Cassini UVIS Interplanetary Hydrogen Ly α Observations from 1999 to 2017, *ApJ*, **960**, 117
- Quémerais, E., & Bertaux, J.-L. 1993, Radiative Transfer in the Interplanetary Medium at Lyman α , *A&A*, **277**, 283
- Quémerais, E., & Bertaux, J.-L. 2002, Radiometric Calibration of the SWAN Instrument, in The Radiometric Calibration of SOHO, ed. A. Pauluhn, M. C. E. Hubbard, & R. von Steiger (Bern: ISSI), 203
- Quémerais, E., Chaufray, J.-Y., Koutroumpa, D., et al. 2020, PHEBUS on Bepi-Colombo: Post-launch Update and Instrument Performance, *SSRv*, **216**, 67
- Quémerais, E., Izmodenov, V., Koutroumpa, D., & Malama, Y. 2008, Time Dependent Model of the Interplanetary Lyman α Glow: Applications to the SWAN Data, *A&A*, **488**, 351
- Swaczyna, P., McComas, D. J., Zirnstein, E. J., et al. 2020, Density of Neutral Hydrogen in the Sun's Interstellar Neighborhood, *ApJ*, **903**, 48
- Thomas, G. E. 1978, The Interstellar Wind and Its Influence on the Interplanetary Environment, *AREPS*, **6**, 173
- Tobiska, W. K., Woods, T., Eparvier, F., et al. 2000, The SOLAR2000 Empirical Solar Irradiance Model and Forecast Tool, *JASTP*, **62**, 1233
- Tobiska, W. K., & Bower, S. D. 2006, New Developments in SOLAR2000 for Space Research and Operations, *AdSpR*, **37**, 347
- Vondrak, R., Keller, J., Chin, G., & Garvin, J. 2010, Lunar Reconnaissance Orbiter (LRO): Observations for Lunar Exploration and Science, *SSRv*, **150**, 7
- Witt, N., Ajello, J. M., & Blum, P. W. 1979, Solar Wind Latitudinal Variations Deduced from Mariner 10 Interplanetary H (1216 A) Observations, *A&A*, **73**, 272
- Witte, M. 2004, Kinetic Parameters of Interstellar Neutral Helium: Review of Results Obtained During One Solar Cycle with the Ulysses/GAS-instrument, *A&A*, **426**, 835
- Woods, T. N., Tobiska, W. K., Rottman, G. J., & Worden, J. R. 2000, Improved Solar Lyman α Irradiance Modeling from 1947 through 1999 Based on UARS Observations, *JGR*, **105**, 27195